Elastic Averaging in Flexure Mechanisms: A Three-Beam Parallelogram Flexure Case Study

Shorya Awtar[1]
e-mail: awtar@umich.edu

Kevin Shimotsu

Shiladitya Sen

Mechanical Engineering,
University of Michigan,
2350 Hayward Street,
Ann Arbor, MI 48109

Redundant constraints are generally avoided in mechanism design because they can lead to binding or loss in expected mobility. However, in certain distributed-compliance flexure mechanism geometries, this problem is mitigated by the phenomenon of elastic averaging. Elastic averaging is a design paradigm that, in contrast with exact constraint design principles, makes deliberate and effective use of redundant constraints to improve performance and robustness. The principle of elastic averaging and its advantages are illustrated in this paper by means of a three-beam parallelogram flexure mechanism, which represents an overconstrained geometry. In a lumped-compliance configuration, this mechanism is prone to binding in the presence of nominal manufacturing and assembly errors. However, with an increasing degree of distributed-compliance, the mechanism is shown to become more tolerant to such geometric imperfections. The nonlinear elastokinematic effect in the constituent beams is shown to play an important role in analytically predicting the consequences of overconstraint and provides a mathematical basis for elastic averaging. A generalized beam constraint model is used for these predictions so that varying degrees of distributed compliance are captured using a single geometric parameter. The closed-form analytical results are validated against finite element analysis, as well as experimental measurements. [DOI: 10.1115/1.4002204]

Keywords: elastic averaging, constraint-based design, overconstraint, flexure mechanisms, beam constraint model, elastokinematic effect

1 Introduction and Motivation

Exact constraint design (ECD), also known as kinematic design, has been the cornerstone of rigid-link mechanism analysis and synthesis [1–13]. The key guiding principle in this paradigm is to employ exactly the minimum number of constraints that are needed to produce the desired mobility or degrees of freedom (DoFs). ECD ensures predictable and repeatable motions, eliminates any possibility of binding, and allows cost-effective fabrication of mating components. In contrast, mechanism geometries that employ redundant constraints, also known as overconstrained geometries, are often prone to undesired internal loads and binding.

The rationale for avoiding redundant constraints, even when they are apparently nonconflicting, lies in the ideal constraint characteristics of traditional rigid-link mechanisms: The links are perfectly rigid, the joints are infinitely stiff in their constraint directions, while offering zero resistance in their DoF directions, and the joints are free of looseness or backlash. These idealizations are indeed closely maintained even in the physical embodiments of rigid-link mechanisms. The parallelogram mechanism of Fig. 1(*a*), without the middle link, would be exactly constrained with the two parallel rigid links, each connecting the ground to the coupler via two revolute joints. One way to describe the mobility of this mechanism is to say that the coupler has one translational DoF along the transverse direction, as shown in this figure. When a third rigid link (shown dashed) is added between the ground and coupler, this one DoF is preserved only if the three links are "perfectly" parallel. Otherwise, the DoF count will drop to zero, as formally predicted by Grubler's criterion [14], which does not account for special geometries.

This three-link parallelogram mechanism (Fig. 1(*a*)) is clearly overconstrained. The distinctive feature of this arrangement is that its mobility is critically dependent on its geometric accuracy, making it highly sensitive to manufacturing tolerances and environmental variations. The slightest loss of parallelism between the three links would lead to a geometry that can move only if small displacements along the length of the links were allowed. The latter is impossible given the infinite translational stiffness of the rigid links and the revolute joints. This would lead to binding or a loss in mobility, as predicted above by Grubler's criterion. Thus, overconstrained rigid-link arrangements are feasible only when the manufacturing accuracy is extremely high, or if the revolute joints are loose enough to accommodate any residual manufacturing errors.

Given this common-sense rationale for ECD, it has also been extended to the design of flexure mechanisms (also known as compliant mechanism), which comprise rigid and compliant elements [12,13,15]. Motion in a flexure mechanism arises from the elastic deformation of the compliant elements instead of sliding or rolling [11–13,16,17]. The resulting lack of friction and backlash provides smooth motion and an exceptional level of precision. The monolithic construction of flexure mechanisms also leads to design simplicity and maintenance-free operation even in harsh environments. In spite of these benefits, flexure mechanisms exhibit several performance trade-offs that arise from their nonideal constraint behavior [17,18]. Parallelogram flexure mechanisms with a single translational DoF are shown in shown in Fig. 1(*b*) (lumped compliance) and Fig. 1(*c*) (distributed compliance). These are commonly used as linear guides or bearings to provide approximate straight line motion in various applications

[1]Corresponding author.

Contributed by the Mechanisms and Robotics Committee of ASME for publication in the JOURNAL OF MECHANISMS AND ROBOTICS. Manuscript received November 12, 2009; final manuscript received July 6, 2010; published online September 30, 2010. Assoc. Editor: G. K. Ananthasuresh.

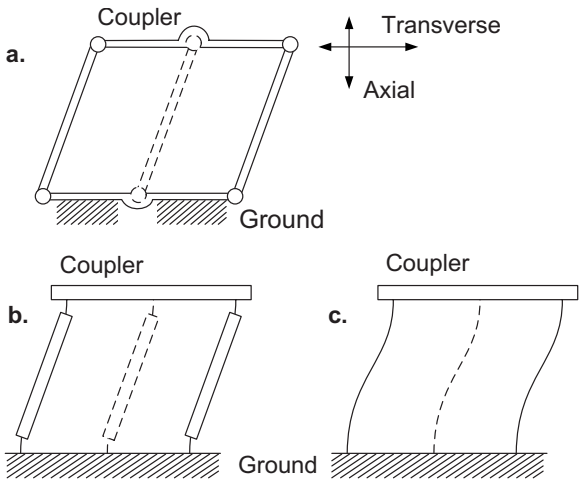

Fig. 1 Parallelogram mechanism: (*a*) traditional linkage, (*b*) lumped-compliance flexure, and (*c*) distributed-compliance flexure

[11–13,16–18]. Following ECD guidelines, let us initially consider these mechanisms with only two beams each. For these mechanisms to serve as motion guides, it is generally desirable to maximize their load-bearing stiffness along the axial direction, while keeping the transverse stiffness as low as possible to minimize stresses and maximize range along their single translational DoF. While the lumped-compliance configuration provides better axial stiffness, its transverse stiffness is also relatively high. This leads to greater actuation effort, higher stresses, and reduced range of motion along the DoF. DoF motion range is improved in the distributed-compliance configuration, which provides a better distribution of strains and therefore lower stresses. But now the axial stiffness is also reduced, which limits the load-bearing capacity. Any attempt to increase this axial stiffness by increasing the flexure beam thickness results in a cubic order increase in the transverse stiffness, which is obviously undesirable. These performance trade-offs seen in the lumped and distributed-compliance geometries are inherent to flexure mechanisms [18].

Contradicting ECD guidelines, if one were to introduce a "perfectly" parallel third beam (dashed line) in either of the parallelogram flexure mechanisms of Fig. 1(*b*) or Fig. 1(*c*), there would be a proportional increase in the transverse and axial stiffness values. Thus, the introduction of additional beams clearly helps overcome the above performance trade-offs. But the question that remains is whether the problems associated with overconstraint, described earlier, are applicable here or not. It may be qualitatively argued that overconstraint will likely be a problem for the lumped-compliance configuration (Fig. 1(*b*)) since the flexural pivots preclude the possibility of "loose" joints and also provide relatively high translational stiffness. Any deviation from perfect parallelism can still lead to an unexpectedly high stiffness and potential binding in the transverse or DoF direction. However, in the three-beam distributed-compliance configuration of Fig. 1(*c*), the axial stiffness of each individual beam is relatively lower and therefore the resulting increase in the transverse stiffness of the mechanism, in case of geometric imperfections, is also relatively small. Consequently, binding or mobility loss may be avoided. It is therefore no surprise that distributed-compliance multibeam parallelogram flexure mechanism design has indeed been employed in the past [19–21].

This ability of distributed-compliance topologies to tolerate overconstrained geometric arrangements without binding, even in the presence of small geometric imperfections, is known as elastic averaging [8–12,21–25]. While elastic averaging is not a new idea and has been exploited occasionally to achieve greater performance in mechanisms and machines, its treatment so far has been largely empirical or qualitative [26–30]. To enable a wider adoption of elastic averaging, this paper provides a systematic and mathematical basis that helps answer some key design questions such as the following: When is elastic averaging applicable in flexure mechanism design? How large geometric imperfections can be tolerated in an overconstrained flexure mechanism without risking binding? How does one quantify the presence and benefits of elastic averaging?

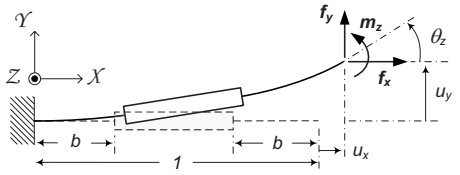

Fig. 2 Generalized beam flexure

Such questions are addressed in this paper in the context of the three-beam parallelogram flexure mechanism. Section 2 provides a generalized parametric beam constraint model that captures the constraint characteristics (stiffness and error motion) of a variable cross-section beam flexure. This model accommodates varying degrees of distributed compliance via a single geometric parameter and captures relevant geometric nonlinearities. In Sec. 3, the generalized beam constraint model is used to develop the closed-form load-displacement relations for a three-beam parallelogram flexure with a nominal geometric imperfection. In addition to confirming the qualitative arguments behind elastic averaging, these closed-form analytical results provide new physical and quantitative insight into overconstraint in flexure mechanisms. The design of a novel, reconfigurable experimental set-up to test various geometric configurations of the three-beam parallelogram flexure is presented in Sec. 4. The closed-form analytical results are validated via comparison with finite element analysis and experimental measurements in Sec. 5. The contributions of this paper are summarized in Sec. 6.

2 Background: Beam Constraint Model for a Variable Cross Section Beam

To study elastic averaging in the three-beam parallelogram flexure mechanisms of Figs. 1(*b*) and 1(*c*), it is first important to establish the constraint properties of the beam flexure. This has been previously accomplished via a beam constraint model [18,31], a brief summary of which is provided here. Figure 2 illustrates an initially straight, variable cross section beam in its undeformed and deformed states with normalized end-loads ($\boldsymbol{f_x}$, $\boldsymbol{f_y}$, and $\boldsymbol{m_z}$) and end-displacements (u_x, u_y, and θ_z) along the *X-Y-Z* coordinate frame. Displacements and lengths are normalized by the overall beam length L, forces by EI_{zz}/L^2, and moments and strain energy by I_{zz}/L. All normalized quantities are scalar and are represented by lower case letters throughout this paper; additionally, all loads (forces/moments) are represented by bold letters. E represents Young's modulus of the material for an *XY* plane-stress condition and the plate modulus for an *XY* plane-strain condition. I_{zz} represents the second moment of area of the two compliant end-segments, each of length b, thickness t, and depth h. The middle section of the beam is thick enough to be considered rigid. The geometric parameter b quantifies the degree of distributed compliance: $b=1/2$ represents a simple beam with uniformly distributed compliance, while $b\rightarrow 0$ corresponds to a lumped-compliance configuration.

Clearly, the transverse directions Y and Θ represent DoFs, while the axial direction X represents a degree of constraint (DoC). The beam constraint model (BCM) comprises parametric nonlinear load-displacement and strain energy relations for the beam:

$$\begin{Bmatrix} f_y \\ m_z \end{Bmatrix} = \begin{bmatrix} k_{11}^{(0)} & k_{12}^{(0)} \\ k_{12}^{(0)} & k_{22}^{(0)} \end{bmatrix} \begin{Bmatrix} u_y \\ \theta_z \end{Bmatrix} + f_x \begin{bmatrix} k_{11}^{(1)} & k_{12}^{(1)} \\ k_{12}^{(1)} & k_{22}^{(1)} \end{bmatrix} \begin{Bmatrix} u_y \\ \theta_z \end{Bmatrix} + f_x^2 \begin{bmatrix} k_{11}^{(2)} & k_{12}^{(2)} \\ k_{12}^{(2)} & k_{22}^{(2)} \end{bmatrix} \times \begin{Bmatrix} u_y \\ \theta_z \end{Bmatrix} \tag{1}$$

$$u_x = \frac{f_x}{k_{33}} - \frac{1}{2}\{u_y \quad \theta_z\} \begin{bmatrix} k_{11}^{(1)} & k_{12}^{(1)} \\ k_{12}^{(1)} & k_{22}^{(1)} \end{bmatrix} \begin{Bmatrix} u_y \\ \theta_z \end{Bmatrix} - f_x \{u_y \quad \theta_z\} \begin{bmatrix} k_{11}^{(2)} & k_{12}^{(2)} \\ k_{12}^{(2)} & k_{22}^{(2)} \end{bmatrix} \begin{Bmatrix} u_y \\ \theta_z \end{Bmatrix} \tag{2}$$

$$v = \frac{1}{2}\frac{f_x^2}{k_{33}} + \frac{1}{2}\{u_y \quad \theta_z\} \begin{bmatrix} k_{11}^{(0)} & k_{12}^{(0)} \\ k_{12}^{(0)} & k_{22}^{(0)} \end{bmatrix} \begin{Bmatrix} u_y \\ \theta_z \end{Bmatrix} - \frac{1}{2} f_x^2 \{u_y \quad \theta_z\} \begin{bmatrix} k_{11}^{(2)} & k_{12}^{(2)} \\ k_{12}^{(2)} & k_{22}^{(2)} \end{bmatrix} \begin{Bmatrix} u_y \\ \theta_z \end{Bmatrix} \tag{3}$$

The BCM is based on the Euler–Bernoulli and linearized beam-curvature assumptions. Furthermore, the application of load equilibrium in the deformed beam state leads to the presence of the axial load f_x in the transverse load-displacement relation (1), the geometric constraint relation (2), and the strain energy relation (3). All three relations initially exist as infinite series in the axial load f_x but are truncated in a mutually consistent fashion to retain only the relevant powers of f_x in the BCM [32].

In relation (1), the first matrix captures elastic stiffness, while the second matrix captures load-stiffening, which quantifies the change in DoF direction stiffness in the presence of a constraint load. The third matrix is included to maintain consistency with the following two relations. In relation (2), the first term represents the elastic stretching of the beam. The second term, which represents a kinematic component, arises from the geometric constraint of constant beam arc length and is exclusively dependent on the transverse displacements u_y and θ_z. The third term, also arising from beam arc-length conservation, depends on the transverse displacements, as well as the axial load, and is therefore referred to as the elastokinematic component. This term is unique to distributed-compliance configurations and results in an additional compliance along the constraint direction that increases quadratically with the DoF displacements. Relation (3) presents a nonlinear strain energy expression for the beam that is compatible with the first two relations.

The nondimensional coefficients k in relation (1) are functionals of the beam shape and are referred to as the beam characteristic coefficients. These coefficients are identified via a subscript that highlights their respective location in the stiffness matrix that relates the transverse loads and displacements, and a superscript that denotes the power of axial load f_{x1} in the transverse load-displacement relation that the coefficient are associated with. It is noteworthy that the same coefficients repeat in relations (2) and (3), which highlights the fact that these three relations are fundamentally inter-related [32]. For the limiting case of a simple beam (uniform thickness and initially straight) given by $b=0.5$, these beam characteristic coefficients assume the following numerical values listed in Table 1.

For a generalized beam shape with $b<0.5$, these characteristics coefficients have been analytically derived previously [18]. Only those that are relevant for the subsequent discussion is this paper are listed below:

$$k_{11}^{(0)} = \frac{6}{b(3-6b+4b^2)}$$

$$k_{11}^{(2)} = \frac{-2b^3(105-630b+1440b^2-1480b^3+576b^4)}{175(3-6b+4b^2)^3}$$

$$k_{33} = \frac{1}{2b}\left(\frac{12}{t^2}\right) \tag{4}$$

Table 1 Beam characteristic coefficients for a simple beam

$k_{11}^{(0)}$	12
$k_{12}^{(0)}$	−6
$k_{22}^{(0)}$	4
$k_{11}^{(1)}$	6/5
$k_{12}^{(1)}$	−1/10
$k_{22}^{(1)}$	2/15
$k_{11}^{(2)}$	−1/700
$k_{12}^{(2)}$	1/1400
$k_{22}^{(2)}$	−11/6300

These coefficients are plotted in Fig. 3 (for $t=0.002413$) to illustrate their dependence on the degree of distributed compliance (b). Such a graphical visualization proves to be helpful in interpreting the results associated with elastic averaging in Sec. 3. Overall, relations (1)–(4) provide a single model for beams with any desired degree of distributed compliance, captured simply via the geometric variable b.

3 Three-Beam Parallelogram Flexure Mechanism

A three-beam parallelogram flexure mechanism comprising ground, motion stage, and three "nominally" parallel beams is illustrated in Fig. 4. Although simple beams are shown for clarity, this discussion and analytical treatment are equally valid for the generalized beam discussed in Sec. 2. While beams 1 and 2 are assumed perfectly parallel, a parallelism error α is introduced at beam 3. Angle α simulates a typical manufacturing or assembly imperfection, for example, a 1 mm parallelism error over 100 mm beam length. This provides an estimate of the maximum magnitude of α that might be of interest: 0.01. Consequently, the small angle approximations $\cos\alpha \approx 1$ and $\sin\alpha \approx \alpha$ are applicable. The normalized loads f_x, f_y, and m_z applied at point O on the motion stage result in normalized displacements x, y, and θ at the same point. The normalization scheme followed here is the same as described above.

As discussed in Sec. 1, the presence of three beams makes this mechanism geometry overconstrained. If the beams were all perfectly parallel, one would expect 1 DoF (Y direction displacement) and 2 DoCs (X direction displacement and Θ direction rotation). However, if beam 3 (or any other, for that matter) is

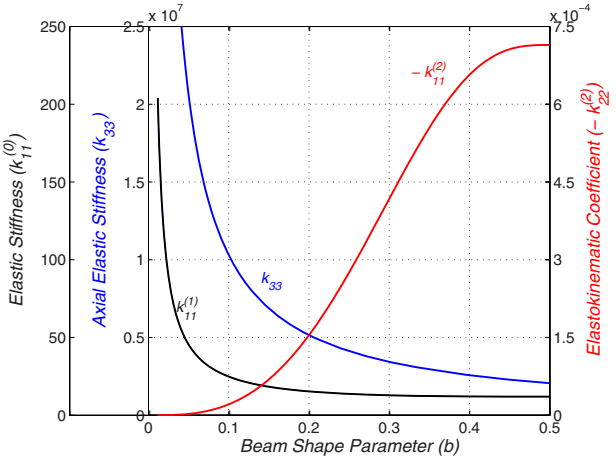

Fig. 3 Beam characteristic coefficients versus beam shape

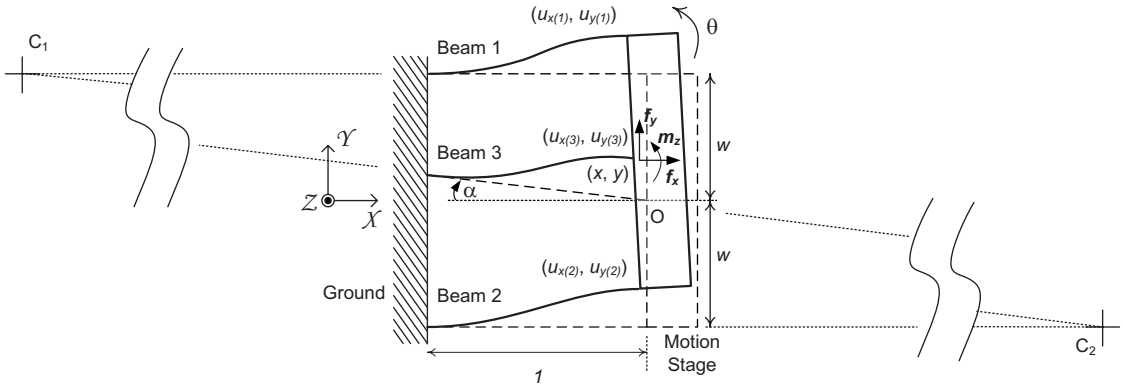

Fig. 4 Three-beam parallelogram flexure with a geometric error

slightly angled, then a potential loss in mobility can be physically visualized. In the present case, the arrangement of beam 1, beam 3, and the motion stage provides a remote center of rotation at C_1 for the motion stage [18]; on the other hand, beam 2, beam 3, and the motion stage result in a remote center of rotation located at C_2. Thus, upon the application of a Y direction force at the motion stage, one part of the mechanism works to make the motion stage rotate counterclockwise about point C_1, while the other part tries to make it rotate clockwise about C_2. This obviously imposes conflicting geometric requirements on the motion stage. If the constraint provided by each beam were close to ideal, i.e., high stiffness in the beam's respective constraint (or axial) direction, then the Y DoF direction stiffness of the overall mechanism would also increase, potentially leading to binding. The remainder of this section provides a closed-form analytical corroboration of this qualitative argument.

In the presence of beams 1 and 3 only, the motion stage rotation would be approximately given by $y\alpha/w$, whereas beams 2 and 3, by themselves, would produce $-y\alpha/w$ [18]. Therefore, it is reasonable to assume that the actual motion stage rotation will be bounded as follows:

$$-\frac{y\alpha}{w} < \theta < \frac{y\alpha}{w} \tag{5}$$

Since we are generally interested in a DoF motion range within ± 0.1, the above inequality implies that the motion stage rotation should be of the order of 0.001 or less. Thus, the small angle approximations $\cos\theta \approx 1$ and $\sin\theta \approx \theta$ are also justified here. With this knowledge, we proceed to state the conditions of geometric compatibility between the three beams by expressing the end-displacements of each beam (measured along their local coordinate axes aligned with the undeformed state of the respective beam) in terms of the motion stage displacements:

$$\text{Beam 1: } u_{x(1)} \approx x - w\theta, \quad u_{y(1)} = y - w(1-\cos\theta) \approx y, \quad \theta_{z(1)} = \theta$$

$$\text{Beam 2: } u_{x(2)} \approx x + w\theta, \quad u_{y(2)} = y + w(1-\cos\theta) \approx y, \quad \theta_{z(2)} = \theta$$

$$\text{Beam 3: } u_{x(3)} = x\cos\alpha - y\sin\alpha \approx x - y\alpha,$$
$$u_{y(3)} = y\cos\alpha + x\sin\alpha \approx y - x\alpha, \quad \theta_{z(3)} = \theta \tag{6}$$

A direct analysis of this problem would involve solving 12 equations simultaneously: the three constitutive load-displacement relations (1) and (2) for each beam and the three load equilibrium conditions for the motion stage. Assuming the three externally applied loads ($\boldsymbol{f_x}, \boldsymbol{f_y}$, and $\boldsymbol{m_z}$) to be known, the 12 unknowns in the problem are the three internal end-loads for each beam and the three motion stage displacements (x, y, and θ). Solving these 12 nonlinear equations is mathematically tedious and involves solving for the 9 internal end-loads, which are irrelevant to the final results. Instead, an energy approach based on the principle of virtual work is employed here to avoid the internal loads altogether and considerably reduce the mathematical complexity [32].

Since the shape of each beam is considered identical, the strain energy associated with the ith beam may be determined by substituting the beam axial force obtained from Eq. (2) into Eq. (3).

$$v_i = \frac{1}{2}k_{33}\frac{\left(u_{x(i)} + \frac{1}{2}\{u_{y(i)} \quad \theta_{z(i)}\}\begin{bmatrix} k_{11}^{(1)} & k_{12}^{(1)} \\ k_{12}^{(1)} & k_{22}^{(1)} \end{bmatrix}\begin{Bmatrix} u_{y(i)} \\ \theta_{z(i)} \end{Bmatrix}\right)^2}{\left(1 - k_{33}\{u_{y(i)} \quad \theta_{z(i)}\}\begin{bmatrix} k_{11}^{(2)} & k_{12}^{(2)} \\ k_{12}^{(2)} & k_{22}^{(2)} \end{bmatrix}\begin{Bmatrix} u_{y(i)} \\ \theta_{z(i)} \end{Bmatrix}\right)} + \frac{1}{2}\{u_{y(i)} \quad \theta_{z(i)}\}\begin{bmatrix} k_{11}^{(0)} & k_{12}^{(0)} \\ k_{12}^{(0)} & k_{22}^{(0)} \end{bmatrix}\begin{Bmatrix} u_{y(i)} \\ \theta_{z(i)} \end{Bmatrix} \tag{7}$$

The total strain energy is simply the sum of the strain energies of the individual beams, which may be obtained by substituting Eqs. (6) into Eq. (7). The principle of virtual work then dictates

$$\delta(v_1 + v_2 + v_3) = \delta w = \boldsymbol{f_x}\delta x + \boldsymbol{f_y}\delta y + \boldsymbol{m_z}\delta\theta \tag{8}$$

Since x, y, and θ are independent displacement coordinates in this problem, the coefficients of their variations in the above equation may be identically set to zero to obtain load-displacement relations for the X, Y, and Θ directions. The X direction relation is given by

$$\boldsymbol{f_x} = \frac{k_{33}}{\left(1 - k_{33}\{y \quad \theta\}\begin{bmatrix} k_{11}^{(2)} & k_{12}^{(2)} \\ k_{12}^{(2)} & k_{22}^{(2)} \end{bmatrix}\begin{Bmatrix} y \\ \theta \end{Bmatrix}\right) \times \left[\frac{3}{2}\{y \quad \theta\}\begin{bmatrix} k_{11}^{(1)} & k_{12}^{(1)} \\ k_{12}^{(1)} & k_{22}^{(1)} \end{bmatrix}\begin{Bmatrix} y \\ \theta \end{Bmatrix} + (3x - y\alpha)\right]} \tag{9}$$

This result may be used to express the Y and Θ direction relations in more concise forms:

$$\boldsymbol{f_y} = 3(k_{11}^{(0)}y + k_{12}^{(0)}\theta) + \boldsymbol{f_x}\left(k_{11}^{(1)}y + k_{12}^{(1)}\theta - \frac{\alpha}{3}\right) + \frac{1}{3}\boldsymbol{f_x}^2(k_{11}^{(2)}y + k_{12}^{(2)}\theta) + \frac{k_{33}}{\left(1 - k_{33}\{y \quad \theta\}\begin{bmatrix} k_{11}^{(2)} & k_{12}^{(2)} \\ k_{12}^{(2)} & k_{22}^{(2)} \end{bmatrix}\begin{Bmatrix} y \\ \theta \end{Bmatrix}\right)} \cdot \frac{2}{3}y\alpha^2 + (k_{11}^{(2)}y + k_{12}^{(2)}\theta) \cdot \frac{(k_{33})^2\left(2\theta^2w^2 + \frac{2}{3}y^2\alpha^2\right)}{\left(1 - k_{33}\{y \quad \theta\}\begin{bmatrix} k_{11}^{(2)} & k_{12}^{(2)} \\ k_{12}^{(2)} & k_{22}^{(2)} \end{bmatrix}\begin{Bmatrix} y \\ \theta \end{Bmatrix}\right)^2} \tag{10}$$

$$m_z = 3(k_{12}^{(0)}y + k_{22}^{(0)}\theta) + f_x(k_{12}^{(1)}y + k_{22}^{(1)}\theta) + \frac{1}{3}f_x^2(k_{12}^{(2)}y + k_{22}^{(2)}\theta) + \frac{k_{33}}{\left(1 - k_{33}\{y \quad \theta\}\begin{bmatrix} k_{11}^{(2)} & k_{12}^{(2)} \\ k_{12}^{(2)} & k_{22}^{(2)} \end{bmatrix}\begin{Bmatrix} y \\ \theta \end{Bmatrix}\right)} \cdot 2\theta w^2 + (k_{11}^{(2)}y + k_{12}^{(2)}\theta) \cdot \frac{(k_{33})^2\left(2\theta^2 w^2 + \frac{2}{3}y^2\alpha^2\right)}{\left(1 - k_{33}\{y \quad \theta\}\begin{bmatrix} k_{11}^{(2)} & k_{12}^{(2)} \\ k_{12}^{(2)} & k_{22}^{(2)} \end{bmatrix}\begin{Bmatrix} y \\ \theta \end{Bmatrix}\right)^2} \tag{11}$$

Since θ is of the order of 0.001 or less for y of the order of 0.1, the former may be dropped with respect to the latter in the above relations, incurring errors less than 1%. This simplifying assumption reduces relation (9) to

$$x \approx \frac{f_x}{3k_{33}} - \frac{1}{2}k_{11}^{(1)}y^2 - \frac{f_x}{3}k_{11}^{(2)}y^2 + \frac{y\alpha}{3} \tag{12}$$

In this expression, the first term may be identified to be the purely elastic component of the axial displacement, the second term represents the purely kinematic component, the third term represents the elastokinematic component, and the last term represents a new kinematic term arising from the geometric imperfection.

Since we are interested primarily in the Y direction load-displacement characteristics, in addition to the above simplification we can also set $m_z = f_x = 0$ without loss in generality. This helps further simplify the mathematical relation (10), so as to allow some physical insight:

$$f_y \approx 3k_{11}^{(0)}y + \frac{2}{3} \cdot \left(\frac{k_{33}}{1 - k_{33}k_{11}^{(2)}y^2}\right) \cdot y\alpha^2 + \frac{2}{3} \cdot \left(\frac{k_{33}}{1 - k_{33}k_{11}^{(2)}y^2}\right)^2 \cdot k_{11}^{(2)}y^3\alpha^2 \tag{13}$$

Differentiation with respect to y yields the DoF direction stiffness of the three-beam parallelogram flexure with a small parallelism error α, for any given degree of distributed compliance captured via variable b:

$$\frac{\partial f_y}{\partial y} = 3k_{11}^{(0)} + \frac{2}{3} \cdot \left(\frac{k_{33}}{1 - k_{33}k_{11}^{(2)}y^2}\right) \cdot \alpha^2 - \frac{10}{3} \cdot \left(\frac{k_{33}}{1 - k_{33}k_{11}^{(2)}y^2}\right)^2 k_{11}^{(2)}y^2\alpha^2 + \frac{8}{3} \cdot \left(\frac{k_{33}}{1 - k_{33}k_{11}^{(2)}y^2}\right)^3 (k_{11}^{(2)})^2y^4\alpha^2 \tag{14}$$

Since the force and displacement values in this expression are normalized with respect to EI/L^2 and L, respectively, it presents a nondimensional stiffness that is normalized with respect to EI/L^3. The beam characteristic coefficients that appear in this expression are $k_{11}^{(0)}$, $k_{11}^{(2)}$, and k_{33}. Referring to Eq. (1), $k_{11}^{(0)}$ is the linear elastic Y-direction bending stiffness of an individual beam (for zero or negligible θ). Referring to Eq. (2), k_{33} is the linear elastic X-direction axial stiffness of an individual beam and $k_{11}^{(2)}$ represents the elastokinematic effect in this direction associated with y displacement (for zero or negligible θ). The effective X-direction compliance, resulting from the elastic and nonlinear elastokinematic effects, is given by $(1/k_{33} - k_{11}^{(2)}y^2)$, and stiffness is simply the inverse of this. Figure 3 illustrates that with increasingly lumped-compliance, $k_{11}^{(0)}$ gradually grows to infinity. Similarly, the normalized axial stiffness k_{33} also grows to infinity, but at an even faster rate. Apart from its dependence on beam shape parameter b, k_{33} also increases quadratically[2] with decreasing beam thickness t. The elastokinematic coefficient $k_{11}^{(2)}$, which is a unique attribute of distributed-compliance configurations, expectedly reduces with decreasing values of b and, in fact, approaches zero asymptotically for b less than 0.1. We would like to note here that the previously reported [21] expression for the Y direction stiffness is incorrect because of premature truncation. Since $k_{33}k_{11}^{(2)}y^2$ is generally not small with respect to 1, an infinite series expansion and truncation are not justifiable.

For nominal mechanism dimensions ($w = 0.5$) and beam thickness ($t = 0.002413$), a series of Y direction stiffness plots, based on Eq. (14), over a range of beam shapes and imperfection angles are presented in Fig. 5. Based on these results, several important observations can be made:

1. In the absence of a geometric imperfection ($\alpha = 0$), the Y stiffness simply reduces to $3k_{11}^{(0)}$. The effect of beam shape parameter b on this nominal stiffness is captured in relation (4).

2. In the presence of small but finite α, a purely linear result (valid only for $y \to 0$) may be obtained by dropping the higher power y terms in Eq. (13):

$$f_y \approx \left(3k_{11}^{(0)} + \tfrac{2}{3} \cdot k_{33}\alpha^2\right)y \tag{15}$$

This shows that the axial stiffness k_{33} of the individual beams is reflected in the Y DoF direction due to the geometric imperfection. Consequently, the effective stiffness in the DoF direction is higher than the nominal stiffness and grows as a quadratic function of α, as may be seen at $y = 0$ for various beam shapes in Figs. 5(*a*)–5(*c*). With decreasing b, since k_{33} increases at a much faster rate than $k_{11}^{(0)}$ (see Fig. 3), the increase in effective stiffness compared with nominal stiffness is much more significant in the case of lumped compliance compared with disturbed compliance, for the same beam thickness t and geometric error α. For example, Fig. 5(*d*) shows that while the nominal stiffness increases by two times going from a b value of 0.5 to 0.1, the effective stiffness increases by more than four times. This increase in effective DoF stiffness, seen at $y = 0$, is the underlying cause of binding in this overconstrained mechanism and is clearly more prominent in the case of lumped compliance. Thus, the vulnerability of lumped compliance to mobility loss in overconstrained mechanism geometries is clear even in a purely linear analysis.

3. Expressions (13) and (14) show that with increasing y displacement, the elastokinematic nonlinearity results in a reduced constraint (or axial) stiffness of the individual beams: $k_{33}/(1 - k_{33}k_{11}^{(2)}y^2)$ instead of k_{33}, which also leads to a reduction in the DoF direction stiffness of the flexure mechanism. This happens when $-k_{33}k_{11}^{(2)}y^2$ (always a positive quantity) in the denominator becomes of the order of or larger than 1.

For the case of thin beams (high k_{33}) with uniformly distributed compliance, which corresponds to the maximum possible magnitude of $k_{11}^{(2)}$, the quantity $-k_{33}k_{11}^{(2)}y^2$ can become much larger than 1. This leads to the following simplified DoF load-displacement relation:

$$f_y \approx 3k_{11}^{(0)}y + \frac{2}{3} \cdot \left(\frac{k_{33}}{-k_{33}k_{11}^{(2)}y^2}\right) \cdot y\alpha^2 + \frac{2}{3} \cdot \left(\frac{k_{33}}{-k_{33}k_{11}^{(2)}y^2}\right)^2 \cdot k_{11}^{(2)}y^3\alpha^2 = 3k_{11}^{(0)}y$$

This analytical observation is significant. It indicates that in certain cases (when $-k_{33}k_{11}^{(2)}y^2 \gg 1$), the effective stiffness of the three-beam parallelogram flexure with a geometric imperfection comes back down to its nominal stiffness as though there was no

[2]This might appear counterintuitive since the axial beam stiffness increases linearly with beam thickness t. However, k_{33} represents the axial stiffness normalized with respect to the bending stiffness, which leads to an inverse quadratic dependence on t.

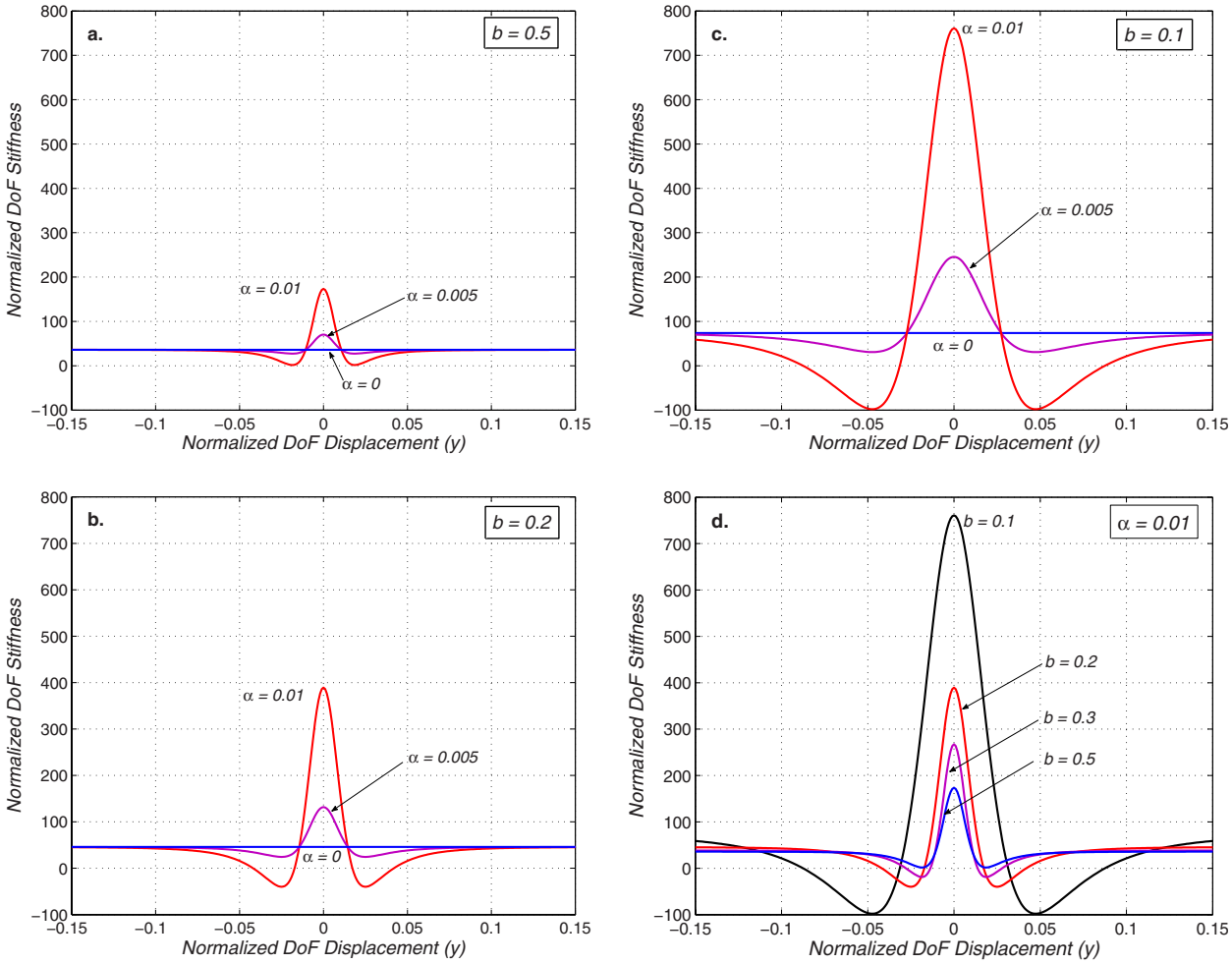

Fig. 5 Analytically predicted *Y*-direction stiffness of the three-beam parallelogram flexure

geometric imperfection. This is evident in the distributed-compliance configuration in Fig. 5(*a*). In other words, because of the elastokinematic effect associated with distributed-compliance, the $-k_{33}k_{11}^{(2)}y^2 \gg 1$ condition is met and the risk associated with binding in the given overconstrained mechanism is mitigated. This phenomenon is elastic averaging.

On the other hand, $-k_{33}k_{11}^{(2)}y^2$ can remain low despite increasing displacements ($y \sim 0.1$) and thin beams (i.e., high k_{33}) if $-k_{11}^{(2)}$ is small, as is the case with lumped-compliance configurations. As per Fig. 3, even though k_{33} increases with decreasing b, the magnitude of the elastokinematic coefficient $k_{11}^{(2)}$ drops and becomes virtually zero for $b < 0.1$. Therefore, there is not much respite in the constraint direction stiffness of the beams even with increasing y displacement, and $k_{33}/(1-k_{33}k_{11}^{(2)}y^2)$ remains close to k_{33}. Thus, not only is the Y DoF effective stiffness in the presence of a geometric imperfection higher in a lumped-compliance configuration, but it also remains high over a larger Y DoF displacement range, as evident in Fig. 5(*d*). The use of thinner beams helps increase k_{33}, but this by itself is not adequate because the elastokinematic coefficient $k_{11}^{(2)}$ also has to be large enough for elastic averaging to kick in and make the mechanism tolerant to geometric imperfections. This observation is further illustrated quantitatively in Table 2 (Sec. 4), which lists several different beam geometries.

Also evident in Fig. 5(*d*) is that for a given geometric error, the effective stiffness undergoes a greater variation in lumped-compliance geometries. For a large enough error and degree of lumped compliance (e.g., $\alpha = 0.01$ and $b = 0.1$), the stiffness is predicted to approach zero and even become negative. This potentially leads to bistability, which is highly undesirable in a linear bearing design. This simply reaffirms the importance and applicability of ECD guidelines in lumped-compliance flexure mechanism geometries. On the other hand, the fact that such a dramatic stiffness variation and resulting bistability does not happen in the corresponding distributed-compliance geometry highlights that ECD guidelines are not strictly applicable in this case. A comprehensive prior-art summary and analytical treatment of multistability in flexure mechanisms is covered in Ref. [33].

4. Ultimately, this discussion highlights that to predict the nature and benefits of elastic averaging in flexure mechanisms, we first have to recognize the elastokinematic nonlinearity in the axial constraint stiffness of the constituent beam: $k_{33}/(1-k_{33}k_{11}^{(2)}y^2)$. Furthermore, for elastic averaging to take place, the condition $-k_{33}k_{11}^{(2)}y^2 \gg 1$ has to hold. In other words, the nonlinear elastokinematic compliance of a beam in the axial direction should be greater than its linear elastic compliance. Thus, the nondimensional quantity $-k_{33}k_{11}^{(2)}y^2$ becomes the mathematical metric for determining whether elastic averaging will play a role in an overconstrained flexure mechanism design or not. This metric is listed for several geometric configurations of the flexure mechanism under consideration in Table 2, Sec. 4. This also highlights the significance of the normalization scheme in this work, which allows a comparison of pertinent mathematical quantities and the relative strength of physical effects.

While k_{33} increases with decreasing b, $k_{11}^{(2)}$ decreases at an even faster rate. However, it is the product of these two that should be

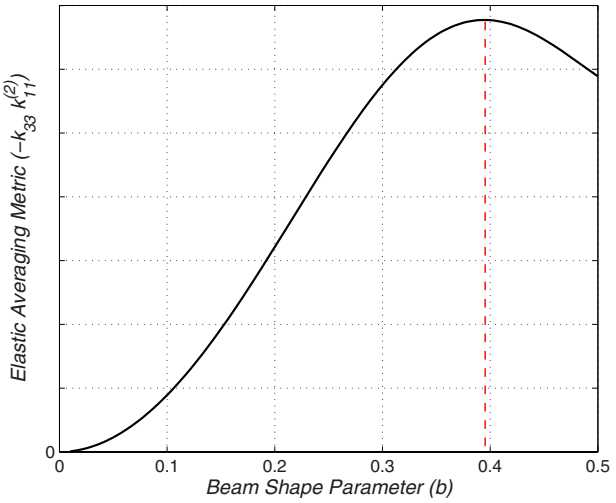

Fig. 6 Elastic averaging metric versus beam shape

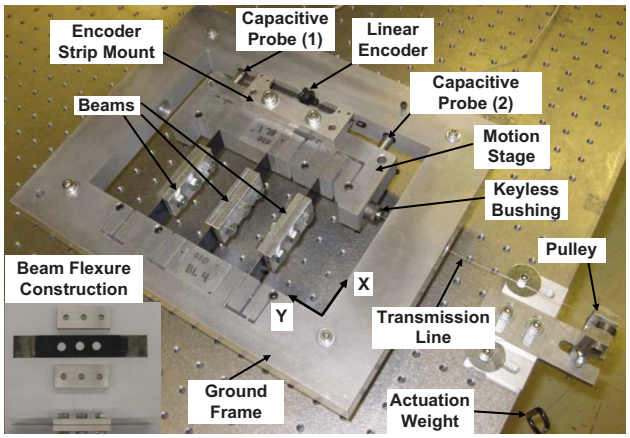

Fig. 7 Reconfigurable three-beam parallelogram flexure experimental set-up

high for elastic averaging to take effect. Figure 6 shows the product $-k_{33}k_{11}^{(2)}$ plotted against the beam shape parameter b. While the beam thickness t affects only the vertical axis scale, which is intentionally omitted, the shape of this curve and location of the maxima ($b=0.4$) remain unchanged. This leads to the so-far unknown and physically nonobvious conclusion that the optimal beam shape for elastic averaging corresponds to $b=0.4$ and not necessarily $b=0.5$. However, since the incremental improvement is small, the latter may still be preferred due to ease of fabrication. It is clear from Fig. 6 that elastic averaging will not play a significant role for smaller values of b, which correspond to lumped-compliance configurations.

5. In a design with only two beams (exact constraint), where binding is not a concern and elastic averaging is not needed, it is noteworthy that the increase in $k_{11}^{(0)}$ with decreasing b is much slower than the increase in k_{33}, even though eventually both grow to infinity (see Fig. 3). This implies that using a beam shape corresponding to $b=0.25$, one can increase the axial stiffness by more than twice while increasing the transverse stiffness only by 10%. However, now if one tries to increase the beam thickness to reduce the stresses due to axial loads or increase the axial stiffness, the transverse stiffness and bending stresses will increase cubically. Bending stresses, in turn, limit the transverse displacement. Adding a third beam of the original thickness not only reduces the axial stress and increases axial stiffness, it also raises the transverse stiffness only by 50% while keeping the bending stresses and transverse motion range the same. Of course, to incorporate a third beam without causing binding, elastic averaging would have to be invoked, which would require a beam with greater distributed compliance ($b\sim0.4$). In fact, more and more beams can be added, while reducing the beam thickness to simultaneously increase the axial stiffness, reduce axial stresses, keep the transverse stiffness and bending stresses under control, and maximize transverse displacements. Thus, elastic averaging helps overcome some of the fundamental performance trade-offs seen in flexure mechanisms, and this benefit can now be quantified based on the above mathematical framework.

For the sake of completeness, we continue from expression (11) to find the motion stage rotation θ, which is a parasitic error motion in this case. Given its small magnitude, second and higher powers of θ may be dropped. Setting $\boldsymbol{f}_x=\boldsymbol{m}_z=0$, without loss in generality, yields

$$\theta \approx \frac{-\left[3k_{12}^{(0)}y+\left(\frac{k_{33}}{1-k_{33}k_{11}^{(2)}y^2}\right)^2\cdot\frac{2}{3}k_{11}^{(2)}y^3\alpha^2\right]}{\left[\left(\frac{k_{33}}{1-k_{33}k_{11}^{(2)}y^2}\right)\cdot 2w^2+\left(\frac{k_{33}}{1-k_{33}k_{11}^{(2)}y^2}\right)^2\cdot\frac{2}{3}k_{12}^{(2)}y^2\alpha^2\right]} \tag{16}$$

Once again, the contribution of the elastokinematic nonlinearity is evident here. The limiting cases of $\alpha=0$, $-k_{33}k_{11}^{(2)}y^2\gg1$, or $-k_{33}k_{11}^{(2)}y^2\ll1$ could be considered to further simplify the above expression and obtain physical insight into the behavior of this parasitic rotation.

4 Experimental Set-Up Design

In order to experimentally validate the above analytical load-displacement results in a comprehensive fashion, it was deemed necessary to test several geometric configurations with varying beam thicknesses (t), manufacturing imperfection angles (α), and degree of distributed compliance (b). The measurement objective was to record the X, Y, and Θ displacements of the motion stage in response to known Y direction actuation forces. However, making a separate prototype for each configuration would obviously be impractical and cost-prohibitive. Therefore, we designed a highly reconfigurable experimental set-up, illustrated in Fig. 7, that accommodates all of the above variations.

Blue-tempered spring steel (ASTM A682, AISI 1095) shim-stock was chosen for the beam material because of its high strength to modulus ratio ($S_y=455$ MPa, $E=205$ GPa, and $\nu=0.3$). For a nominal beam length $L=100$ mm, readily available thicknesses ($T=0.2413$ and 0.635 mm) were chosen to ensure that a Y displacement of ±10 mm ($y=\pm0.1$) could be achieved with an adequate margin of safety against yielding. For ease of fabrication, a standard out-of-plane dimension (beam height) of $H=25.4$ mm and a beam spacing of $W=50$ mm were selected. Along with the nominal case of $\alpha=0$, two geometric imperfection angles, $\alpha=0.0035$ and 0.007, were considered for this study. The last number represents a 0.7 mm parallelism error over a 100 mm beam length. Although most well-controlled macroscale manufacturing and assembly processes are capable of producing better tolerances, we decided to include potential misalignments that might arise in case of a human error, large volume productions, or in microfabrication. Since the objective here is to understand elastic averaging in the context of lumped and distributed compliance, several levels of distributed compliance were considered ($b=0.5$, 0.3, 0.2, and 0.1). While keeping the beam spacing W, beam

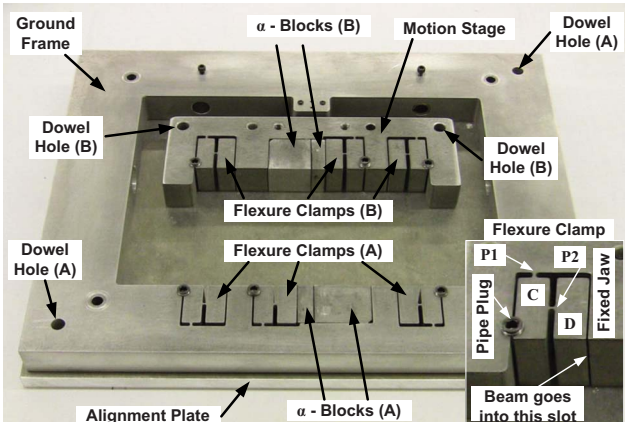

Fig. 8 Alignment and assembly of the ground frame and motion stage

height H, and material E invariant, the various geometric configurations that result from the above described variations are compiled in Table 2.

All quantities listed in this table are nondimensionalized. Values of the k coefficients are simply obtained from relations (4) and may be seen in Fig. 3. In the final column, the product $-k_{11}^{(2)}k_{33}y^2$, which was identified as a metric for elastic averaging in Sec. 3, is listed for a y displacement of 0.1. The greater this number with respect to 1, the less vulnerable is the associated geometric configuration to binding in the presence of geometric imperfections.

In the proposed experimental set-up, a single set of ground frame and motion stage, shown in Fig. 8, accommodate all the beam variations. Three flexure clamps (A) are monolithically incorporated in the ground frame and another three flexure clamps (B) are incorporated in the motion stage. These flexure clamps allow an easy assembly and disassembly of the individual beam flexures with the ground frame and motion stage. Each of these flexure clamps (Fig. 8, inset), first reported in Ref. [17], includes a flat clamping surface or fixed jaw, two flexure pivots P1 and P2, rigid block C, rigid block D, and a pipe plug. Tightening the pipe plug, which has tapered threads, causes block C to rotate about pivot P1. This by itself would have provided poor clamping action against the fixed jaw because of a localized contact. However, pivot P2 in this clamp design accommodates the rotation of block C, while transmitting only a translation to block D. This allows block D, which serves as the moving jaw, to remain parallel to the fixed jaw and provide a uniformly distributed clamping force on a beam that goes in between the two jaws. This results in a clamped joint that is easy to secure or release and is free of backlash. This clamp design also helps align the beam with respect to the fixed jaw, while the moving jaw aligns itself to conform to the beam. A gap of 0.75 mm was left between the fixed and moving jaws of each clamp to accommodate the largest beam thickness (T =0.635 mm).

Next, the imperfection angle α of the middle beam was achieved using a set of four fixture blocks, referred to hereafter as the α-blocks. Two α-blocks (A) interface with the middle flexure clamp of the ground frame, while the other two α-blocks (B) interface with the middle flexure clamp of the motion stage. Each of these blocks have one face lined up against either the moving or fixed jaw of its associated flexure clamp, and an opposing face that is precision machined to be at an angle α with respect to the first face. One end of the middle beam gets sandwiched between the two angled faces of two α-blocks (A), which in turn are sandwiched between the moving and fixed jaws of the middle clamp on the ground frame. A similar arrangement is repeated on the motion stage, as shown in Fig. 8. With the use of a separate set of α-blocks for each angle, we were able to create and test multiple cases of geometric imperfection (α=0, 0.0035, and 0.007). For this arrangement to work effectively, the ground frame, motion stage, the α-blocks, and the beam flexures have to be assembled in the correct position and orientation. To accomplish this, an alignment plate (Fig. 8) was employed to build up the assembly. This plate has two pairs of dowel pins pressed in precise locations corresponding to slide-fit holes (A) and (B) on the ground frame and motion stage, respectively. The first step in the assembly is to

Table 2 Geometric variations of the three-beam parallelogram flexure

α	b	$k_{11}^{(0)}$	$k_{11}^{(2)}$ ($^*10^{-3}$)	k_{33}	$-k_{11}^{(2)}k_{33}y^2$
		Thickness T=0.2413 mm, t=0.002413			
0	0.5	12.00	−1.429	2,060,946	29.45
0	0.3	12.82	−0.838	3,434,910	28.78
0	0.2	15.31	−0.312	5,152,365	16.08
0	0.1	24.59	−0.043	10,304,730	4.43
0.0035	0.5	12.00	−1.429	2,060,946	29.45
0.0035	0.3	12.82	−0.838	3,434,910	28.78
0.0035	0.2	15.31	−0.312	5,152,365	16.08
0.0035	0.1	24.59	−0.043	10,304,730	4.43
0.007	0.5	12.00	−1.429	2,060,946	29.45
0.007	0.3	12.82	−0.838	3,434,910	28.78
0.007	0.2	15.31	−0.312	5,152,365	16.08
0.007	0.1	24.59	−0.043	10,304,730	4.43
		Thickness T=0.635 mm, t=0.00635			
0	0.5	12.00	−1.429	297,601	4.25
0	0.3	12.82	−0.838	496,001	4.16
0	0.2	15.31	−0.312	744,001	2.32
0	0.1	24.59	−0.043	1,488,003	0.64
0.0035	0.5	12.00	−1.429	297,601	4.25
0.0035	0.3	12.82	−0.838	496,001	4.16
0.0035	0.2	15.31	−0.312	744,001	2.32
0.0035	0.1	24.59	−0.043	1,488,003	0.64
0.007	0.5	12.00	−1.429	297,601	4.25
0.007	0.3	12.82	−0.838	496,001	4.16
0.007	0.2	15.31	−0.312	744,001	2.32
0.007	0.1	24.59	−0.043	1,488,003	0.64

locate the ground frame and motion stage on the alignment plate via these dowel pins and holes. Next, the two outer beams are inserted into their respective clamps, and the middle beam is inserted into the middle clamps along with the α-blocks. All these components rest on the flat alignment plate. Once the flexure clamps have been tightened, the entire assembly is carefully lifted off the alignment plate and mounted on an optics table using four pillars.

The ground frame, motion stage, and the α-blocks were made from a 1 in. (25.4 mm) thick AL6061-T651 plate using wire electric discharge machining (wire-EDM), to maintain dimensional, flatness, and angular tolerances associated with the flexure clamps and α-blocks.

Flexure beams that slide into the appropriate clamps on the ground frame and motion stage were designed to have a Z-direction height ($H=25.4$ mm) that matches the height of the rest of the components. To vary the beam shape, we employed 6.32 mm thick and 25.4 mm high rigid AL-6061 plates that could be bolted to the center of the spring steel strips (Fig. 7, inset). For $b=0.5$, the spring steel strip was used by itself for the beams, and for all other values of b, the spring steel strip was sandwiched between appropriately sized rigid plates.

To measure the Y displacement of the motion stage with respect to the ground frame, a noncontact linear optical encoder (42 μm resolution), shown in Fig. 7, was used because of its unrestricted motion range, zero-friction, simple mounting and set-up, noise-free digital output data, and low-cost. For measuring the X and Θ direction parasitic error motions of the motion stage, we employed two noncontact capacitance probes mounted on the ground frame, as shown in Fig. 7. These probes are ideally suited for this purpose for several reasons: The range of motion to be measured is small (<0.6 mm), the probes are tolerant to the relatively large Y DoF motion perpendicular to their measurement axes, and the achievable resolution ($\sim$40 nm) is more than adequate. Each probe was mounted in the ground frame via a bronze bushing that is split along its length and is held in place via a radial set-screw. The bushing helps distribute the force from the set-screw uniformly over the probe length, thus preventing any damage to the probe surface and associated loss of calibration.

Y actuation of the motion stage was achieved using free hanging weights applied in increments of 5–10 g, and measured separately to within 0.1 g. A keyless bushing was used to attach a nylon fishing line to one end of the motion stage; this fishing line passed through a hole on the side of the ground frame, and then over a low-friction pulley attached to the optics table. The keyless bushing provides an easily attachable and detachable friction-based clamp that is free backlash. The motion stage and the keyless bushing mounting hole in it were designed such that the Y-direction actuation force would pass through the modeled point O on the motion stage (see Fig. 4). Since free weights can provide actuation loads in only one direction, the same actuation set-up was provided on both ends of the motion stage and ground frame to allow bidirectional testing.

5 Analytical and Experimental Results

In addition to BCM based close-form analysis and experimental measurements, extensive finite element analysis (FEA) was also conducted in ANSYS to provide yet another prediction of the three-beam parallelogram flexure's load-displacement behavior for all the geometric configurations listed in Table 2. BEAM4 elements were used with consistent matrix and large displacement options (NLGEOM) turned on and shear coefficients set to zero. The beam flexures were meshed using up to 10 elements per mm of the beam length. The convergence criterion for all cases was set to a relative tolerance limit of 0.001 on the L2 norm of the forces.

Analytical predictions based on the BCM (line) and FEA (circles) along with experimental measurements (crosses), of the normalized Y actuation force versus normalized Y displacement, are plotted in Fig. 9 for a representative subset of the various geometric configurations considered. These results reveal a good agreement between the BCM based analytical predictions, FEA, and experimental measurements. For any beam shape, for example $b=0.2$ in Figs. 9(g), 9(d), and 9(a), it is clear that the effective stiffness at small displacements ($y\rightarrow 0$) increases from a nominal value with increasing α. However, due to elastic averaging, this effective stiffness comes back down to the nominal stiffness value, as though α were zero, with increasing displacements. This is best seen in the cases with high α (Figs. 9(a)–9(c)), where the force-displacement curve asymptotically approaches a linear analysis prediction at small displacements, and reverts to the nominal stiffness at large displacements. Both asymptotes are highlighted via dotted lines in Figs. 9(a)–9(c). A nonlinear transition region between the effectiveness stiffness and nominal stiffness regimes is also evident.

For the same increase in angular imperfection, the increase from nominal to effective stiffness is the more prominent for $b=0.2$ (Figs. 9(g), 9(d), and 9(a)) compared with $b=.5$ (Figs. 9(i), 9(f), and 9(c)). This confirms that lumped-compliance configurations are more prone to stiffness increase, and potential binding, in the DoF direction. Moreover, the transition from the effective stiffness regime to the nominal stiffness regime in the maximum imperfection angle case is the smoothest for $b=0.5$ (Fig. 9(c)) and goes through a stronger nonlinear behavior for $b=.2$ (Fig. 9(a)). This shows that distributed compliance configurations are better at rejecting the detrimental effects of geometric imperfection.

Overall, the BCM prediction closely follows the FEA prediction for all cases, proving the effectiveness of the proposed nonlinear closed-form parametric modeling approach. The only deviation that occurs is in the transition region between the effective stiffness and nominal stiffness regimes for cases with high geometric imperfection and low distributed compliance (Fig. 9(a)). The reason for this deviation lies in the fact that expression (1) in the BCM is truncated to the second power of the axial load f_{x1} in what is originally an infinite series [32]. While this truncation provides simplicity to the BCM and allows its use in the closed-form parametric analysis of more complex flexure mechanisms such as the one being considered here, it restricts the validity of the model to normalized axial load values within $-35<f_{x1}<50$ to maintain less than 2% truncation error. In fact, for larger magnitudes, while errors associated with tensile axial loads grow at a small rate, the errors associated with compressive axial loads increase significantly. When the three-beam parallelogram flexure is actuated in the positive direction (see Fig. 4), it may be qualitatively argued that the middle beam will experience a compressive axial load while the two outer beams will see the axial tensile loads. For the geometric configuration of Fig. 9(a) (large α and low b), which is most prone to overconstraint and binding, the compressive load on the middle beam grows with increasing y displacement, exceeding a normalized value of 100 in the transition region. This large compressive load results in the discrepancy seen between the BCM and FEA predictions. With further increase in y displacement, the effective axial stiffness of the middle beam drops because of the elastokinematic effect and therefore the associated compressive axial load drops. This drop ensures that the BCM and FEA start to match again in the large y displacement range. When the flexure mechanism is actuated in the negative Y direction, the middle beam now sees an axial tensile force while the two outer beams experience axial compressive forces. However, since the axial forces are equally divided between the two outer beams, their magnitude is less compared with the previous case. Therefore, the agreement between the BCM and FEA is maintained even in the transition region in the negative Y direction. This qualitatively reasoning behind the noted discrepancy has also been validated analytically.

Similarly, there is an overall good agreement between the experimental measurements and BCM predictions, except for the positive Y direction transition region. Between the experiments

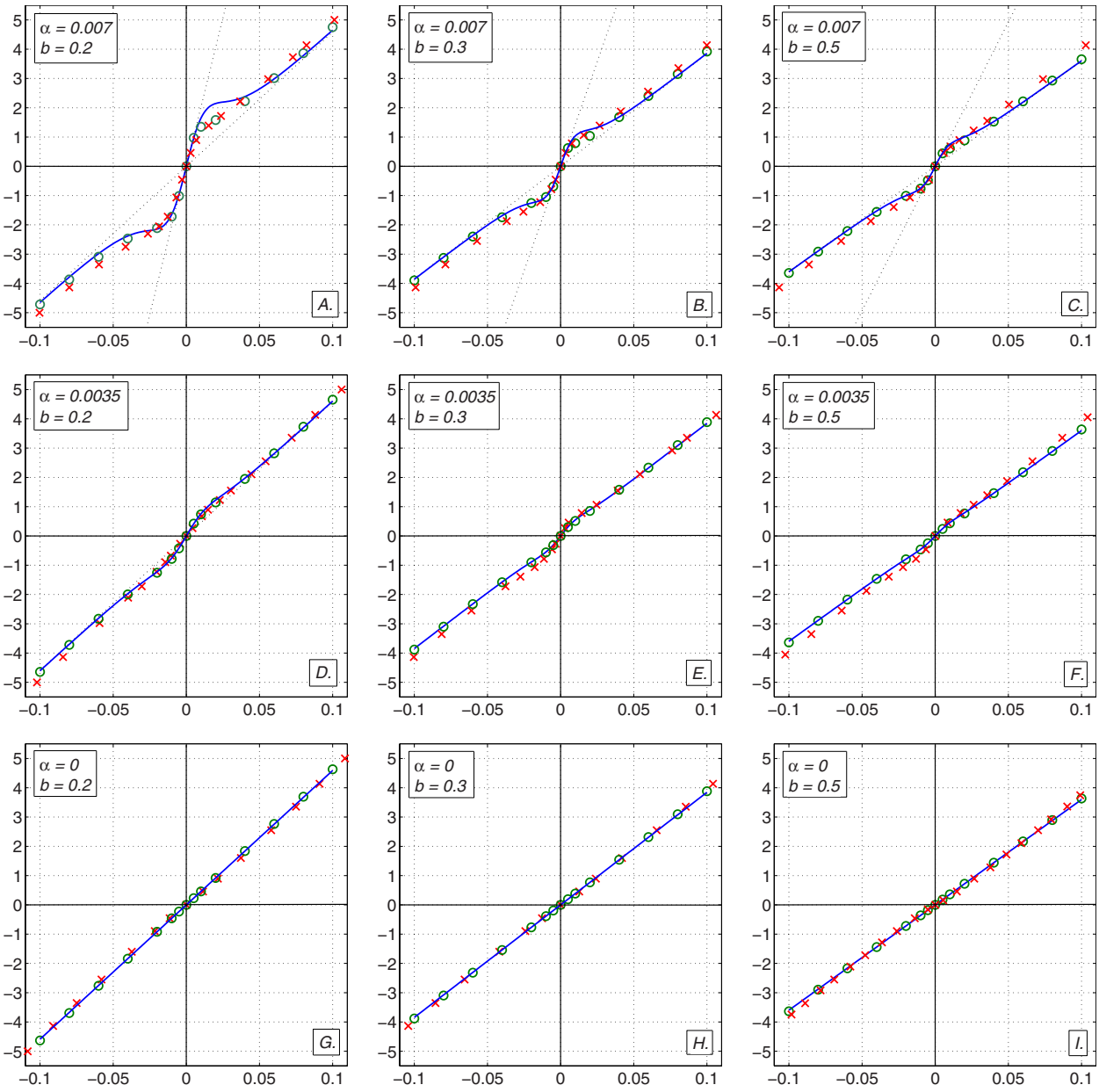

Fig. 9 Normalized *Y* DoF force versus normalized *Y* DoF displacement: BCM (line), FEA (○), and Exp (×)

and FEA, the force-displacement relation trends agree for all cases considered, with a maximum of 5% deviation in the absolute values. This deviation may be attributed to an estimated value of Young's modulus used in the normalization of the experimental data-points (E=205 GPa), as opposed to an actually measured value.

The FEA studies and experimental measurements serve to validate the strength and effectiveness of the BCM in capturing the physical effects in flexures that are pertinent to the systematic and quantitative study of elastic averaging. The discrepancies noted above do not pose a problem because they are restricted to small regions, and the overall DoF direction force-displacement trends are adequately captured. The BCM accurately predicts that even for an overconstrained distributed-compliance mechanism with geometric imperfections, the effective DoF direction stiffness, which might be high at very small displacements, quickly reduces to the nominal stiffness as though there was no geometric imperfection.

To complete the discussion, a comparison between the BCM prediction, FEA prediction, and experimental measurements of the X and Θ direction parasitic error motions of the motion stage is presented in Figs. 10 and 11, respectively, for a representative case (t=0.002413, b=0.2, and α=0.007).

Figure 10 shows a good agreement between the BCM predicted, FEA predicated, and experimentally measured dependence of the X direction displacement on the Y DoF displacement. Both the linear and quadratic components predicted by Eq. (12) are well evident here. Deviations between analysis and experiments are negligible because the relation between the plotted displacements is predominantly kinematic and therefore independent of loads. Figure 11 shows a good agreement between the BCM and FEA predications of the motion stage rotation. However, the experimental measurement of this rotation is an order of magnitude higher and its dependence on the Y DoF displacement is predominantly linear as opposed to the cubic prediction. This deviation is attributable to actual manufacturing tolerances in the experimental set-up. While the two outer beams of the flexure mechanism are

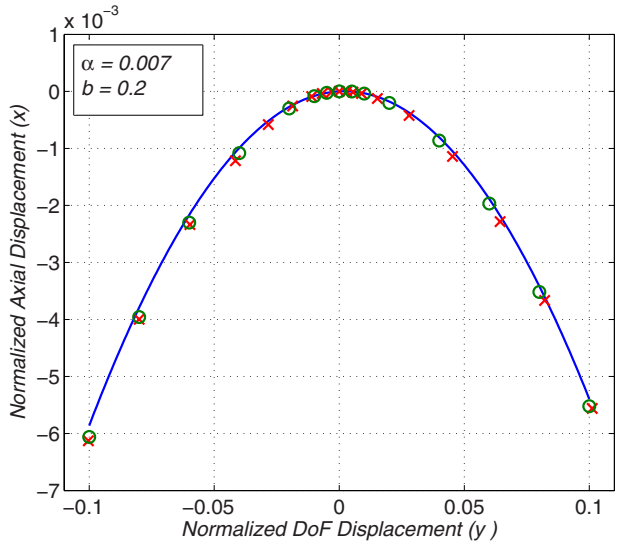

Fig. 10 Normalized *X* displacement: BCM (line), FEA (○), and Exp (×)

assumed to be perfectly parallel to the X axis and equidistant from point O, some deviation, however, small, will still exist in spite of wire-EDM fabrication and careful assembly. It may be analytically shown that while such small deviations do not affect the Y and X direction results, they can significantly affect the Θ rotation, which is a much smaller quantity ($\sim 10^{-4}$) and far more sensitive to the mechanism geometry. An unaccounted angular deviation of 0.0005 rad from perfect zero (which is in the range of wire-EDM tolerances) in either of the outer two beams can lead to a dominant linear effect in the motion stage rotation, of the order of what is seen in the experimental measurements [18].

6 Conclusion

This paper provides a systematic mathematical basis for studying and employing elastic averaging in flexure mechanism design. As a design paradigm, elastic averaging is particularly suited to distributed compliance flexure mechanisms because of their finite constraint direction stiffness, which makes them tolerant to typical manufacturing and assembly errors. This expands the design space to include overconstrained geometries that might be capable of higher performance but are traditionally ruled out by the exact constraint design principles.

Quantitatively, the key highlights of this paper are as follows: (1) A linear analysis shows that geometric imperfections affect lumped-compliance configurations more in terms of an increased effective stiffness in the DoF direction, resulting in a potential mobility loss. (2) Nonlinear analysis is needed to show that the increased effective stiffness comes back to the nominal stiffness with increasing displacements, as though there were no geometric imperfections. This transition is faster and smoother for distributed compliance configurations. (3) The nonlinear elastokinematic effect, along with the linear axial stiffness of the flexure beam, helps define a metric for elastic averaging. The larger this nondimensional number compared with 1, the greater is the resulting mechanism's ability to reject the detrimental effects of geometric imperfections. (4) The nonlinear closed-form load-displacement model of the three-beam parallelogram flexure mechanism is based on the simple yet powerful BCM, which captures elastic, load-stiffening, kinematic, and elastokinematic effects. A generalized BCM that accommodates any beam shape is used here to map the degree of distributed compliance to elastic averaging capability. (5) An energy approach is presented that simplifies the mathematical derivation of force-displacement relations for the mechanism from the BCM. Although a three-beam parallelogram mechanism and a simple parallelism error were considered here to highlight the concept of elastic averaging, the present approach can be readily extended to a parallelogram mechanism with any number of beams and other types of geometric errors. (6) The BCM based closed-form predictions are validated via experimental measurements and FEA.

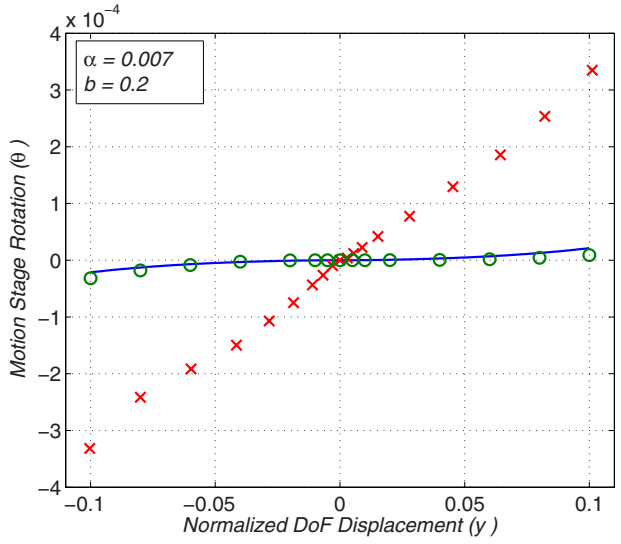

Fig. 11 Motion stage rotation: BCM (line), FEA (○), and Exp (×)

Acknowledgment

This research was supported in part by a National Science Foundation grant (Grant No. CMMI 0846738).

References

[1] Maxwell, J. C., 1980, *The Scientific Papers of James Clerk Maxwell*, Vol. 2, Cambridge University Press, London.
[2] Pollard, A. F. C., 1929, *The Kinematic Design of Couplings in Instrument Design*, Hilger and Watts, London.
[3] Whitehead, T. N., 1934, *The Design and Use of Instruments and Accurate Mechanisms*, Macmillan, New York.
[4] Furse, J. E., 1981, "Kinematic Design of Fine Mechanisms in Instruments," J. Phys. E, **14**, pp. 264–272.
[5] Erdman, A. G., Sandor, G. N., and Kota, S., 2001, *Mechanism Design: Analysis and Synthesis*, Prentice-Hall, Englewood Cliffs, NJ.
[6] Ullman, D. G., 2003, *The Mechanical Design Process*, 3rd ed., McGraw-Hill, New York.
[7] Whitney, D. E., 2004, *Mechanical Assemblies: Their Design, Manufacture, and Role in Product Development*, Oxford University Press, New York.
[8] Whitehouse, D. J., 2003, *Handbook of Surface and Nanometrology*, Institute of Physics, Bristol.
[9] Moore, W. R., 1970, *Foundations of Mechanical Accuracy*, Moore Tool Co., Bridgeport, CT.
[10] Skakoon, J. G., 2008, *The Elements of Mechanical Design*, ASME, New York.
[11] Slocum, A. H., 1992, *Precision Machine Design*, Society of Manufacturing Engineers, Dearborn, MI.
[12] Hale, L. C., 1999, "Principles and Techniques for Designing Precision Machines," Ph.D. thesis, Massachusetts Institute of Technology, Cambridge, MA.
[13] Blanding, D. K., 1999, *Exact Constraint: Machine Design Using Kinematic Principles*, ASME, New York.
[14] Grubler, M., 1917, *Getriebelehre*, Springer, Berlin, Germany.
[15] Hopkins, J. B., 2005, "Design of Parallel Systems via Freedom and Constraint Topologies (FACT)," MS thesis, Massachusetts Institute of Technology, Cambridge, MA.
[16] Jones, R. V., 1988, *Instruments and Experiences: Papers on Measurement and Instrument Design*, Wiley, New York.
[17] Awtar, S., 2004, Analysis and Synthesis of Planer Kinematic XY Mechanisms, Sc.D. thesis, Massachusetts Institute of Technology, Cambridge, MA.
[18] Awtar, S., Slocum, A. H., and Sevincer, E., 2007, "Characteristics of Beam-Based Flexure Modules," ASME J. Mech. Des., **129**(6), pp. 625–639.
[19] Bonin, W. A., 2001, "Microactuator Suspension With Multiple Narrow Beams," U.S. Patent No. 6,282,066.
[20] Trease, B. P., Moon, Y.-M., and Kota, S., 2005, "Design of Large Displacement Compliant Joints," ASME J. Mech. Des., **127**, pp. 788–798.

[21] Awtar, S., and Sevincer, E., 2006, "Elastic Averaging in Flexure Mechanisms: A Multi-Parallelogram Flexure Case-Study," ASME Paper No. 99752.
[22] Wilson, E. B., Jr., 1952, *An Introduction to Scientific Research*, McGraw-Hill, New York.
[23] Jones, R. V., 1962, "Some Uses of Elasticity in Instrument Design," J. Sci. Instrum., **39**, pp. 193–203.
[24] Gardner, J. W., and Hingle, H. T., 1991, *From Instrumentation to Nanotechnology*, Gordon Breach, Philadelphia.
[25] Willoughby, P., 2005, "Elastically Averaged Precision Alignment," Ph.D. thesis, Massachusetts Institute of Technology, Cambridge, MA.
[26] Slocum, A. H., and Weber, A. C., 2003, "Precision Passive Mechanical Alignment of Wafers," J. Microelectromech. Syst., **12**(6), pp. 826–834.
[27] Slocum, A. H., Basaran, M., Cortesi, R., and Anastasios, J. H., 2003, "Linear Motion Carriage With Aerostatic Bearings Preloaded by Inclined Iron Core Linear Electric Motor," Precis. Eng., **27**, pp. 382–394.
[28] Jiang, L., 2007, "A Novel Method for Nanoprecision Alignment in Wafer Bonding Application," J. Micromech. Microeng., **17**(7), pp. S61–S67.
[29] Jurcevich, B. K., 1992, "Structural Mechanics of the Solar—A Soft X-Ray Telescope," Proc. SPIE, **1690**, pp. 399–434.
[30] Awtar, S., and Slocum, A. H., 2007, "Constraint-Based Design of Parallel Kinematic XY Flexure Mechanisms," ASME J. Mech. Des., **129**(8), pp. 816–830.
[31] Awtar, S., and Sen, S., 2010, "A Generalized Constraint Model for Two-Dimensional Beam Flexures: Non-Linear Load-Displacement Formulation," ASME J. Mech. Des., **132**(8), p. 081008.
[32] Awtar, S., and Sen, S., 2010, "A Generalized Constraint Model for Two-dimensional Beam Flexures: Nonlinear Strain Energy Formulation," ASME J. Mech. Des., **132**(8), p. 081009.
[33] Oh, Y. S., 2008, "Synthesis of Multistable Equilibrium Compliant Mechanisms," Ph.D. thesis, University of Michigan, Ann Arbor, MI.